Verifying the HETG spectrometer Rowland design

Michael D. Stage and Daniel Dewey

Center for Space Research
Massachusetts Institute of Technology
Cambridge, MA 02139

ABSTRACT

The HETGS on AXAF is the coordinated operation of the AXAF High-Resolution Mirror Assembly (HRMA), the High-Energy Transmission Grating (HETG), and the grating-readout array of the AXAF CCD Imaging Spectrometer (ACIS-S). XRCF calibration data are analyzed to verify the Rowland geometry design of the HETGS. In particular, ACIS-S imaging of quadrant shutter focus tests is used to probe the focus, alignment, and astigmatism of the spectra produced by diffraction through the high and medium energy gratings (HEGs, MEGs) of the HETG. The experimental results are compared to expected values and to results obtained with the AXAF simulator, MARX.

Keywords: AXAF, HETG, grating, calibration, X-ray, Rowland

1. INTRODUCTION

Extensive testing of NASA's Advanced X-ray Astrophysics Facility(AXAF) occurred at the Marshall Flight Center X-Ray Calibration Facility(XRCF) from December 1996 to April 1997. While a variety of detectors were used with the High Energy Transmission Grating(HETG) during early phases of testing, Phase 2H calibration tested the HETG in flight configuration, using the ACIS-S detector. As part of this testing, the High Resolution Mirror Array(HRMA), the High Energy Transmission Grating(HETG), and the 6 CCD chip spectrometer mode of the ACIS imaging detector(ACIS-S) were combined in flight configuration to form the High Energy Transmission Grating Spectrometer(HETGS). The arrangement is shown in Fig.1. The purpose of this extensive testing was to measure, calibrate, and understand the functioning of the HETGS to determine how well the HETGS meets the design specifications set by the scientific goals for astrophysical x-ray spectroscopy with AXAF. This work can be divided into calibration of the *Effective Area and Efficiency* of the HETGS gratings and mirror assemblage,[1,2] and calibration of the *Point Spread Functions* and *Line Response Function* of the spectrometer.[3] As part of the ongoing characterization of the *Line Response Function*, in this paper we analyze two sets of data designed to verify the geometry of the HETGS. We will simultaneously measure the defocus values of several Medium Energy Grating(MEG) and High Energy Grating(HEG) diffracted orders to confirm the ACIS geometry.

2. THE ROWLAND SPECTROMETER ON AXAF

A detailed discussion of the physics of Rowland spectrographs is beyond the scope of this arcticle. What follows is a brief discussion of the basic principles as they apply to the HETGS. For more detailed accounts, including derivation of grating, astigmatism, Coma, and aberration equations using Fermat's principle, or for specific effects of faceted gratings, please consult the references.[4,5]

In a simple transmission Rowland spectrograph, the gratings and detector are located on opposite sides of the Rowland circle. The location of the images of diffracted orders of a monochromatic source at wavelength λ, for a grating of period p, are:[2,4]

$$sin(\beta) = \frac{m\lambda}{p} \tag{1}$$

It's also useful to note the physical distance from zero order to the m_{th} order, D_{disp}; is given by:

$$D_{\mathrm{disp}} = \left(\frac{m\frac{ch}{E}}{p}\right)(X_{\mathrm{RS}}) = \left(\frac{m\frac{12.398}{E_{\mathrm{keV}}}}{p}\right)(X_{\mathrm{RS}}) \tag{2}$$

Other author information: Send correspondence to M.S.: E-mail: mikstage@space.mit.edu For up to date information, check http://space.mit.edu/HETG/xrcf.html

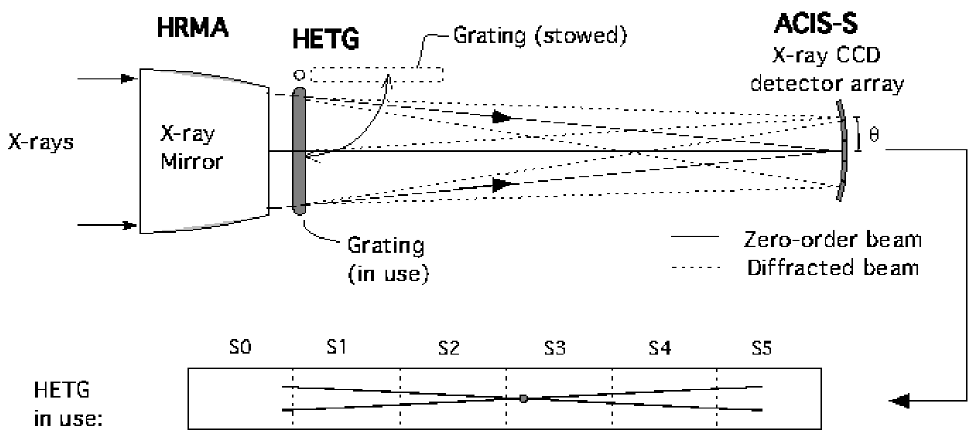

Figure 1. AXAF Optical Path. Xrays are focused by the High Resolution Mirror Array(HRMA), then dispersed by the High Energy Transmission Grating(HETG). The dispersed spectra are imaged by the 6 CCD chip ACIS-S detector.

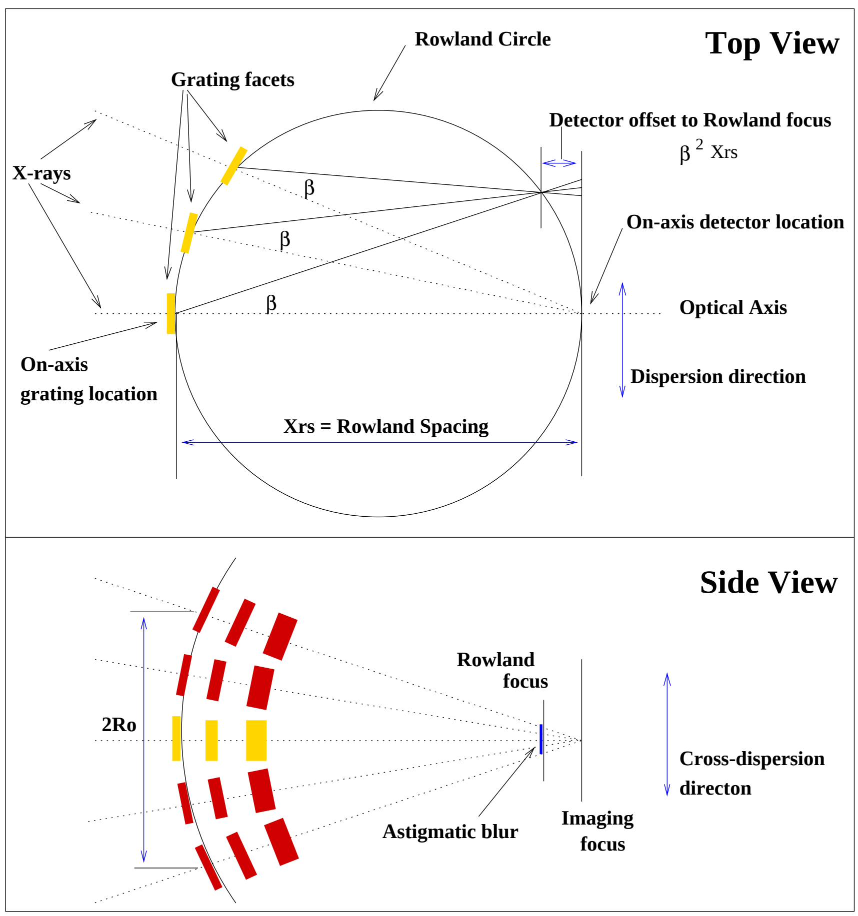

Figure 2. Simplified ray geometry for the Rowland torus design. In the view from above AXAF(Top View), we see the X-rays (dotted lines) already focused by the HRMA to the zero order. The grating facets provide a perturbation to this focus, dispersing the first order spectra at angle β with respect to the optical axis, and bringing the dispersed spectrum to focus on the Rowland circle. From the Side View, we see the cross-dispersion projection of the same rays. Notice that in the cross-dispersion-direction, the rays focus behind the Rowland circle.

We can visualize a simple, one-dimensional Rowland spectrometer by considering the Top View in Fig.2. X-ray light(dotted lines) focussed by the HRMA to image at zero order enters the gratings from the left. The gratings disperse some light to image the $\mathrm{m_{th}}$-order on the Rowland circle at an angle β (black lines). Note the Rowland Spacing, X_{RS}, is the diameter of the Rowland circle and the distance from the gratings to the detector.

Now, consider the Side View in Fig.2. The grey shaded gratings are the same gratings as visible in the Top View, located on the same Rowland circle, now seen in projection. Let us imagine we hold fixed the right side of the circle where it is tangent to the imaging focus plane, and allow the left side to swing above and below the oringinal plane. That is, we rotate the Rowland circle about the dispersion direction axis (visible in Top View, perpendicular to the Side View). In this way, we trace out the additional projected Rowland circles and grating facets shown (black facets). The surface the rotation describes is a *Rowland torus.* Grating facets placed on the torus perpendicular to the converging light rays (dotted lines) will focus diffracted orders on the Rowland circle. Since the Rowland spacing is the same for all grating facets, and the zero order focus coincides for all facets, the m_th diffracted order from each facet is focussed at the same angle β, at the same place on the Rowland circle. That is, best focus for the dispersion direction projection occurs along the inner surface of the Rowland torus, which is approximately along the original (horizontal) Rowland circle.

A basic property of this Rowland design is an astigmatic image. Although best focus in the dispersion direction is along the Rowland circle, the cross-dispersion direction best focus occurs on the axis of revolution of the Rowland torus, in the imaging plane. This can be seen in the Side View in Fig.2. Of course, if we were to flatten the detector to the imaging plane to remove the astigmatism, we would also completely remove the dispersion direction (spectral) imaging ability. Our image would resemble a smeared horizontal line with no spectral information. With a detector curved to follow the Rowland focus, diffracted orders or spectral lines are focussed and sharp in the dispersion direction, and elongated in the cross-dispersion direction. The defocus in the cross-dispersion direction is given by:

$$\delta_{\mathrm{defocus}} = \beta^2 X_{\mathrm{RS}} \tag{3}$$

The HETG is composed of four rings of facets (labeled 1,3,4,6 from the outermost shell inward) which are mounted on the grating superstructure to intercept and diffract the focussed x-rays from the four corresponding HRMA shells (also labeled 1,3,4,6). As the inner shells of HRMA are the most effective for focusing high energy x-rays, the two inner rings of the HETG compose the High Energy Grating, with facets that have a period of 2000Å. The outer rings facets have a period of 4000Å, and make-up the Medium Energy Grating(MEG). The MEG and HEG dispersion axes are rotated slightly with respect to each other, so that the spectra form a flattened "x" in the ACIS image (see Fig.4).

3. DEFOCUS MEASUREMENT APPROACH

In this section, we explain how to measure the defocus of the detector at multiple positions simultaneously by determining a defocus value for each imaged order.

3.1. Determination of Defocus

At XRCF, a shutter system was installed between the HETG and the ACIS-S. Four shutters per HRMA/HETG shell to divide the HETG into quadrants: Top(T), North(N), Bottom(B) and South(S), for a total of sixteen programmable shutters. The dispersion and cross-dispersion direction defocus of a particular order can be found by comparing the position of the imaged order for light from each quadrant.

Fig.3 shows the north and south quadrants of the HETG illuminated. The x-axis runs from the center of the HETG to the center of the ACIS-S detector. The y-axis is the dispersion axis, and the z-axis is the cross-dispersion axis. Note that as a result of the instrument arrangement at XRCF, the Top quadrant(not shown in the diagram) is actually located in the -z half-plane in ACIS-S coordinates, which we will use throughout the rest of this paper. The North quadrant is in the +y half-plane.

For simplicity, we consider the dispersion direction focus of the zero order image. Note that as we trace the x-rays from the HETG towards the focus, the image of the center of the North quadrant, N_y, remains centered on a positive value of y, while S_y remains centered on a negative value of y. This continues until the images meet at the Rowland circle, where they focus at the same value of y. Past the dispersion direction focus, the relative order of the arcs reverses and N_y takes a negative value. The simple geometry of similar triangles allows us to convert

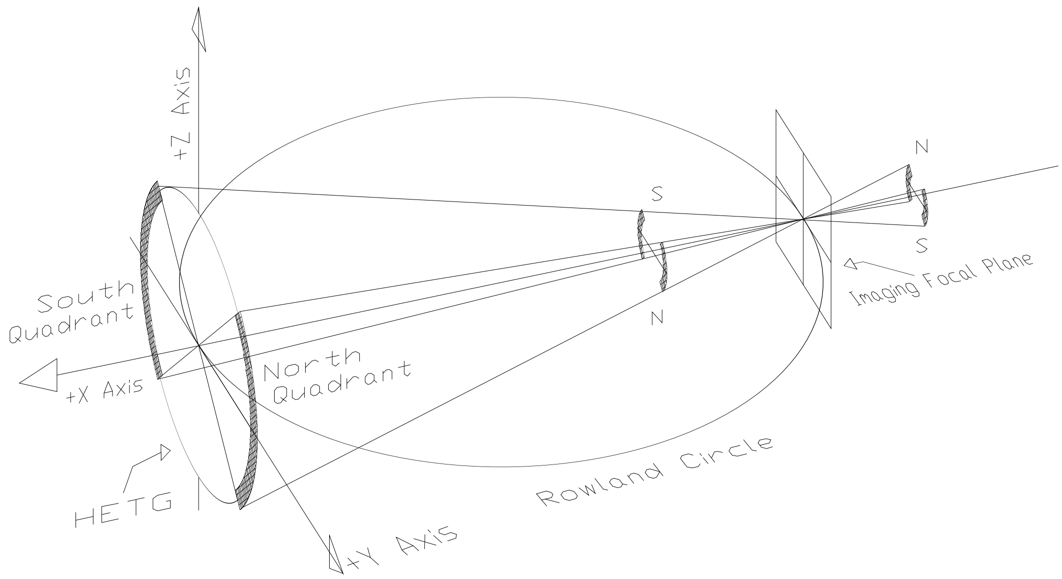

Figure 3. AXAF Quadrant Schematic. X-rays focussed by the HRMA enter from the left, where they are intercepted by the HETG. The shutters for the North and South quadrants are open. We trace the light for zero order to focus on the Rowland circle. For the zero order, the dispersion direction and cross-dispersion direction focii coincide, as the imaging plane (cross-dispersion best focus) is tangent to the rowland circle at zero order. Note that before reaching focus, the center of the N quadrant is located at a more positive value of y than the south quadrant. At dispersion focus on the rowland circle, the orders overlap at the same value. Past focus, this order is reversed.

the difference $N_y - S_y$ into the offset $\mathrm{X_{defocus}}$ from the Rowland circle. The ratio of the offset of the detector to the difference in the location of the arcs is equal to the ratio of the length from the HETG to the detector (the Rowland spacing, X_{RS}), to the separation of the grating arcs on the HETG:

$$\frac{X_{\mathrm{defocus}}}{N_y - S_y} = \frac{X_{\mathrm{RS}}}{2R_{\mathrm{HETG}}} \tag{4}$$

A positive value of $N_y - S_y$ in our image, indicating the detector is displaced towards the HETG, is a positive defocus. Since the value of $N_y - S_y$ will always be positive before focus on the Rowland cicle, and negative past focus, the approach works at all orders.

Although the cross-dispersion direction best focus is located in a different place than the dispersion-direction, the same method is easily used to determine the cross-dispersion defocus at the various orders. We simply replace the $N_y - S_y$ difference with $B_z - T_z$. Of course, since the detector is curved to match the Rowland circle, we expect to find the astigmatic defocus given in 3.

From the symmetry shown in Fig.3, it should be clear that the other two centroid difference measurements, $N_y - S_y$ and $B_z - T_z$, are expected to be zero. Any significant deviations here are likely due to grating or HRMA assymetry. Table 3.1 summarizes the meaning of the four results.

3.2. Real Image Effects

At XRCF, each quadrant was illuminated separately; however, all mirrors were illuminated at once. Consequently, photons from two shell quarter-arcs are in each non-zero MEG and HEG order, and the zero order contains photons from all four shells. In a perfect optical system with no scattering, tiny quarter-arcs would be visible in each imaged order. In reality, mirror scattering perpendicular to the scattering surface obliterates the well-defined arc shapes and create bowties or hourglasses. In this study, the overall defocus was small enough, and the number of events low enough, that even these shapes blurred into small blobs. Bowties are clearly visible in MARX simulations.

Table 1. Quadrant Interpretation

Quadrant Pair	Meaning
N-S, Δ_Y	dispersion (primary) defocus
N-S, Δ_Z	aberrations
B-T, Δ_Z	cross-disp (astigmatic) defocus
B-T, Δ_Y	aberrations

The imaged blob is basically a weighted combination of the centroids of the two quarter-arcs. Correspondingly, in Eqn.(4) we need to consider the separation of the same *weighted centroids* of the rings of the HETG. We replace the real grating radii $R_{\rm HETG}$ with effective radii calculated by weighting the geometric centroids of the quarter arcs with the mirror shell effective areas. Note the HETG radii given in Table 2 are not the actual perpendicular distance from the optical axis to the ring of grating facets, but have been adjusted (by similar triangles) to be the perpendicular height at the full Rowland distance from the detector, intersecting the light ray that travels along the HRMA-HETG-ACIS path.

Table 2. Adjusted Radii of HETG Rings and Mirror Effective Areas

Shell label	HETG Radius[6] $R_\#$ (mm)	Mirror Effective Area $M_\#$ (cm^2)
1	521.66	303.774
3	419.90	211.428
4	370.66	169.467
6	275.44	94.759

To calculate the effective radii, we begin with the geometric centroid of the quarter arc, $C_{\rm QA}$:

$$\frac{C_{\rm QA}}{r} = \left(\frac{5\sqrt{2}}{3+\frac{3\pi}{2}}\right) = .9168453288 \tag{5}$$

Then,

$$R_{\rm Eff,MEG} = \frac{(R_1 A_1 + R_3 M_3) C_{\rm QA}}{M_1 + M_3} \tag{6}$$

$$R_{\rm Eff,HEG} = \frac{(R_4 A_4 + R_6 M_6) C_{\rm QA}}{M_4 + M_6}$$

We derive the following ratios to use in Eqn.(4):

$$\frac{X_{\rm RS}}{2R_{\rm eff,MEG}} = 9.9806 \pm 0.0115 \tag{7}$$

$$\frac{X_{\rm RS}}{2R_{\rm eff,HEG}} = 14.2334 \pm 0.0165$$

The errors in the ratios are based entirely on the error in Rowland diameter; effective area errors were neglected. HETG shell efficiencies were also ignored, as there are considerable uncertainties in HETG efficiency from quadrant to quadrant. Errors in defocus are derived from propagation of statistical and systematic centroid erros and errors in the ratios given above.

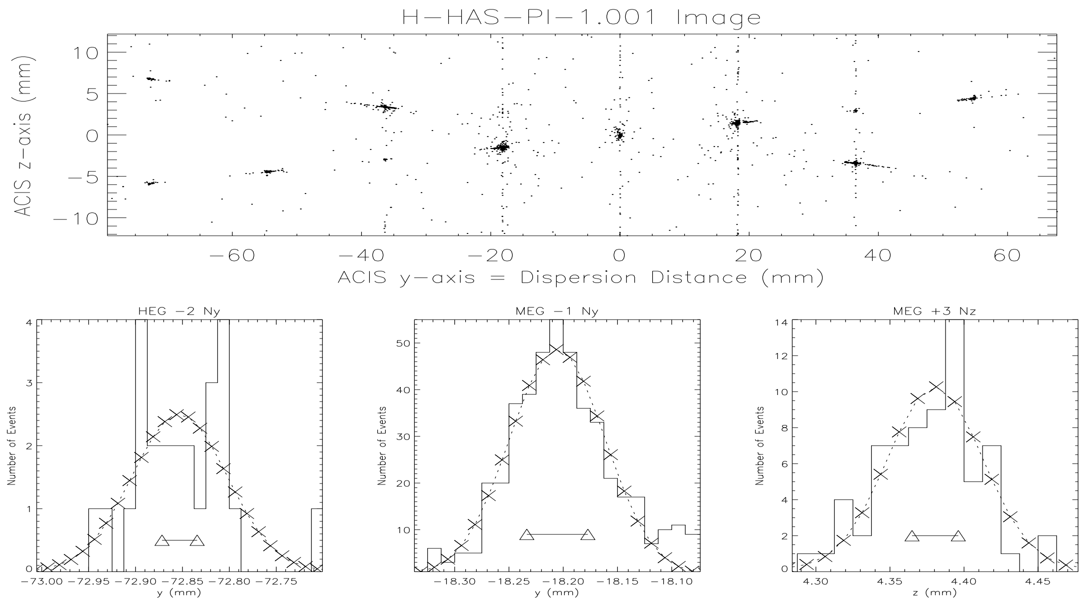

Figure 4. H-HAS-PI-1.001 ACIS-S image and Selected Order Histograms.

4. XRCF DATA ANALYSIS

4.1. XRCF Data & Coordinate Systems

The monochromatic source at XRCF was the Al-K line and contiuum complex at 1.486 keV, and was imaged in the HEG orders -2,-1,0,1 and MEG orders -3,-1,0,1,3 (even orders had very small numbers of events). The data analyzed here are the H-HAS-PI-1.001 and H-HAS-1.003 HRMA-HETG-ACIS-S calibration runs taken at XRCF. The ACIS telemetry was processed by the PSU ACIS team, and we start with their event files for our analysis. In order to facilitate rebinning the data to different bin sizes, the detector integer pixel coordinates are uniformly blurred by ± 0.5 pixels and converted to real-valued distances in millimeters. We further applied PHA to energy conversions and grading. For the analysis here we select events with ASCA grades 0,2,3,4,6 and PHA-energies in the range 1.2 to 1.8 keV. The entire H-HAS-PI-1.001 data set, after grade selection, is shown in Fig.4. The runs are approximately 13ksec and 4ksec. The second run was at a higher source intensity, so the overall numbers of events in a given order and quadrant are roughly comparable, and in fact the higher orders for the 1.003 data contain more events than the 1.001.

The order of quadrant scanning was derived from XRCF log files and determined to be Top, North, Bottom, South. The data are continuous, but the divisions between quadrants were easily determined from examination of the zero order z position data against time. The rms scatter of points from zero order is much greater for the Top and Bottom quadrants than North and South in a Time vs. z scatter plot of events, due to mirror scatter, see discussion in MARX simulation section. Blocks of time for each quadrant were selected to maximize the events counted for each quadrant. The time blocks are very roughly equal. A useful bin size of 12.5μm, approximately half a pixel, was chosen (see Sect. 4.4).

4.2. Calculation of Centroids

To find the y and z centroids of each image blob for each order and quadrant, an IDL program extracted the events in the vicinity of each order for the previously determined time blocks. These events were then histogramed in y and z projection, and the resultant histograms were fit with 1 dimensional Gaussian curves. The parameters of the fit were amplitude, mean (centroid), standard deviation, and a constant background. Two errors were generated for the centroid in an attempt to estimate possible systematic errors. The statistical sigma of the centroid was taken as sigma of the gaussian divided by the square root of the number of events within 4 sigma of the centroid value. In addition, a separate estimate of sigma was calculated as one quarter of the the distance, centered on the centroid mean, which contained 90% of the events in the histogram, as a maximum error covering possible systematic effects.

Examples of three representative fits, for HEG -2, MEG -1 and MEG +3 orders, are given in Fig.4 under the full image. We see the histogrammed data, overlaid with the gaussian fit. The size of the 90% quarter width sigma estimate is given by the horizontal bar capped with triangles. While for order/quadrant combinations with reasonable numbers of events the gaussian fit looks quite reliable, for the HEG -2, and to some extent MEG ± 3 orders the poor numbers of events call into some question the accuracy of the gaussian centroid. Table 3 gives the number of events in each order for H-HAS-PI-1.001. As the HEG -2 histogram indicates, there is considerable fluctuation between bins when only twenty to forty events are binned. With peaks in the histogram at five events, any number of small random effects could distort the fit. We feel; however, that despite such effects almost any independent observer would find the centroid of the histogram to be within a systematic sigma of the gaussian fit mean.

Table 3. Number of Events, per Order, Quadrant. Maxima are typically MEG ± 1 and 0. Minima are generally HEG -2.

Grating	Order	Top	North	Bottom	South
1.001					
HEG	-2	44	29	20	32
HEG	-1	261	204	178	200
HEG	1	242	223	174	214
HEG/MEG	0	441	305	245	318
MEG	-3	54	54	64	63
MEG	-1	617	508	455	570
MEG	1	608	523	414	529
MEG	3	76	72	55	50
1.003					
HEG	-2	37	47	34	71
HEG	-1	240	264	224	272
HEG	1	260	318	223	259
HEG/MEG	0	192	231	139	234
MEG	-3	81	86	84	110
MEG	-1	414	473	372	527
MEG	1	376	417	336	418
MEG	3	99	107	99	95

4.3. Fitting Imaged Order Defocuses

While the imaged orders from a correctly built, correctly aligned HRMA/HETG/ACIS system are easy to interpret, there can be considerable degeneracy in interpreting the results if the quadrant scan indicates defocuses of the various orders and gratings. For example, with an ACIS-S spectrum that is anything less than spectacular, it would be extremely difficult to discriminate between an improperly curved ACIS-S and a slightly misaligned ACIS-S, or in fact even certain problems with the grating or mirror. Fortunately, particularly in the light of the poor statistics of some imaged orders, sub-assembly calibration tests on the HETG[6] and ACIS[7] suggest that we can restrict our attention here to placement issues.

Once the dispersion defocuses are calculated for each imaged order, a linear fit of defocus as a function of dispersion distance can be used as an indicator of Rowland conformance. Linearity indicates correct Rowland curvature. A constant offset indicates the defocus of the entire detector along the optical axis. A statistically significant slope indicates a properly constructed detector which has been placed with a rotation about the z axis. The linear fits to the dispersion defocuses have been plotted in Fig.acis1 for the 1.001 and 1.003 data sets.

The grating provides a minor alteration in the beam to create the dispersion, but the HRMA is primarily responsible for the focus of the photons, so since the MEG and HEG photons originate from different mirror shells, is not unreasonable to expect the MEG and HEG to achieve best (image) focus at different distances. As a result, although somewhat difficult as a result of the small number of orders, the HEG and MEG orders must be fit separately. As it is impossible to separate HEG and MEG photons in the zero order image, it is not used in the fits. As the zero order defocuses are not used in the fits, the zero order defocuses have been plotted as error bars only.

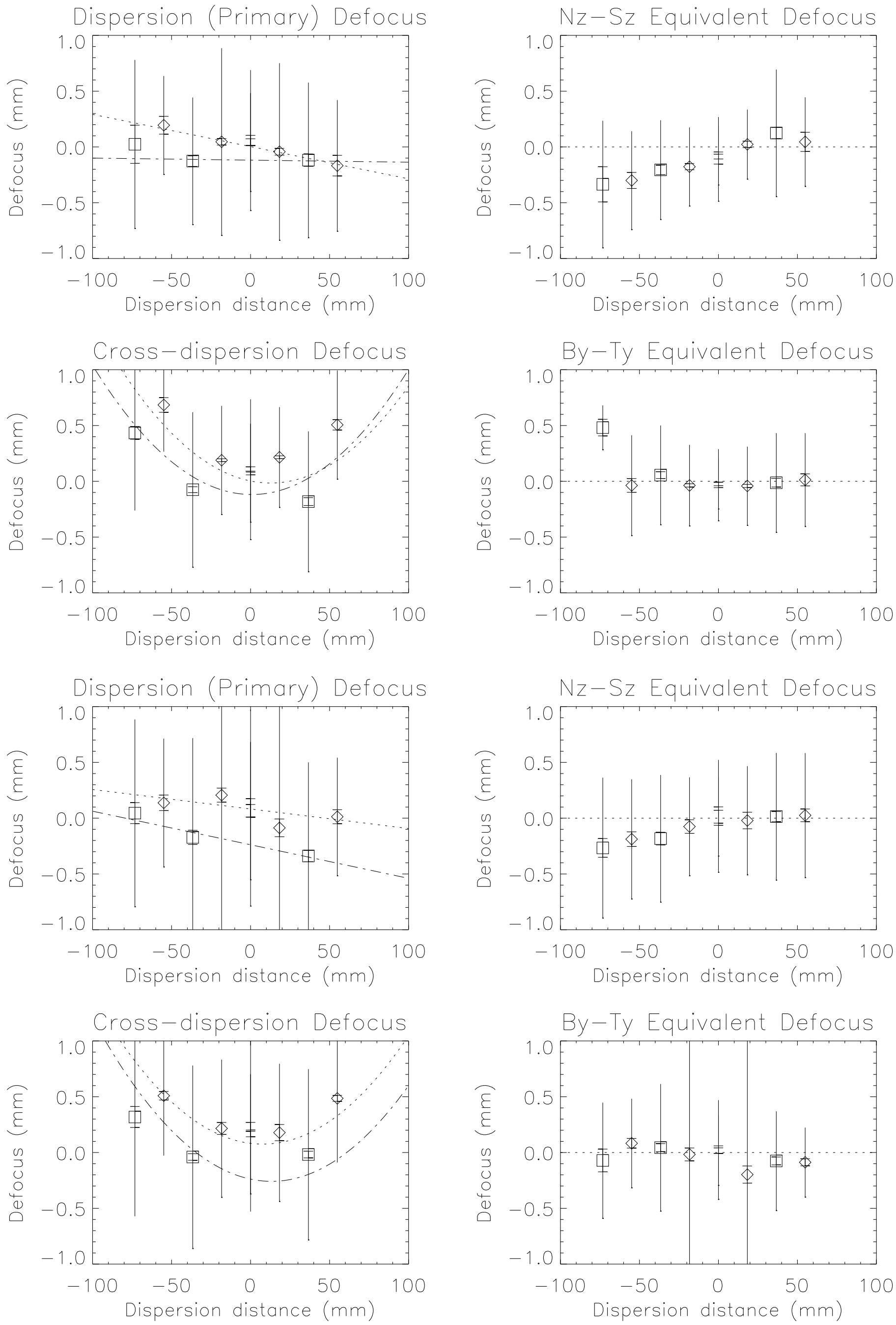

Figure 5. 1.001 and 1.003 Results. Plotted are the defocus values calculated for the four quadrant pair differences. HEG results are plotted as squares and dash-dot lines. MEG results are plotted as triangles and dotted lines. Horizontal cross marks on the error bars indicate the extent of statistical errors; the systematic errors are represented by the continuation of the error bar. The zero orders are not plotted as they are not used in fits; however the zero order error bars have been plotted for comparison. Upper left: Linear fit to dispersion direction defocus gives the overall offset and any rotation (tilt) of the detector about the z axis. Lower left: Cross-dispersion direction (astigmatic) defocus. The curves show the expected values of astigmatic defocus, based on the Rowland circle offset from the imaging focal plane and the detector offsets from the dispersion direction fit. Upper and lower right: Equivalent defocuses for the $N_z - S_z$ and $B_y - T_y$ separations. These points are expected to agree with zero.

The cross-dispersion defocuses can be compared to the expected astigmatic defocus as a function of dispersion distance (see Eqn.(3), plus any overall defocus or rotational defocus calculated from the dispersion defocuses. That is, the inherent astigmatism is modified by adding to it the results of the linear fit, $(overall\ defocus) + (tilt)(D_{\mathrm{disp}})$. In the cross-dispersion direction graphs in Fig.4.3, the results of the dispersion direction fits have been used with the inherent astigmatism to generate curves showing the expected astigmatic blurring. The astigmatic curves for the 1.001 run show marginal agreement for the MEG data points, and somewhat underestimate the defocus of the HEG points. Though perhaps slightly displaced, the shape of the HEG curve seems appropriate for the data. The astigmatic curves for the 1.003 run seem a bit wide, but generally agree in magnitude and shape.

The final two graphs in Fig.4.3 show the $N_z - S_z$ and $B_y - T_y$ differences, converted by similar triangles into a defocus value. A consistent linear fit to the both $N_z - S_z$ and $B_y - T_y$ would indicate an overall rotation of the detector. However, what we see are non-corresponding deviations from zero. Though a trend is visible in the $N_z - S_z$ plots, the lack of a complimentary trend in the T-B delta y plot suggests that if real this is a result of minor aberrations or asymmetries in the HETG/HRMA. The almost total agreement of the points with zero when considering the systematic error bars reminds us however that this may simply be a result of undersampling.

Table 4. Linear Fit Results for 1.001 and 1.003.

Grating Data	Statistical Fit Defocus (mm)	Tilt (arcmin)	Systematic Fit Defocus (mm)	Tilt (arcmin)
MEG				
1.001	0.003 ± 0.020	-9.93 ± 2.72	0.011 ± 0.309	-11.27 ± 22.24
1.003	0.082 ± 0.034	-6.00 ± 2.79	0.075 ± 0.361	-4.33 ± 24.22
HEG				
1.001	-0.118 ± 0.036	-0.63 ± 3.21	-0.109 ± 0.437	-3.33 ± 30.95
1.003	-0.238 ± 0.037	-10.34 ± 2.88	-0.234 ± 0.556	-11.48 ± 36.55

4.4. Tests of Robustness

For certain low-statistics orders, the centroiding process may be sensitive to the bin size. Certain combinations of bin size and order also fail to converge to a gaussian fit. To quantify this as a possible source of error and to generate as accurate an actual centroid as possible, the centroiding process was repeated for bin sizes ranging from 0.004 mm to 0.032 mm. For every bin size which resulted in convergent fits, the centroid locations for each quadrant and order were recorded, and the corresponding number of events in the y and z histograms were recorded. In the same manner as described in the previous sections, a the defocus of each order for each bin size was calculated. Then, the median values for the four defocus measurements for each order were determined. By taking the median value of the calculated defocus over the set of successful bin sizes, we select the the most robust value of the centroid separation under this fitting process (defocus is linear in centroid separation), and avoid difficulties with poorly determined gaussian mean outliers affecting a straight average.

Finally, the median values with errors are used to fit the overall defocus of the detector. The end results of this process are not generally different from choosing an approximately half-pixel bin size.

5. DISCUSSION OF GEOMETRICAL APPROXIMATIONS

There are a number of approximations used in the centroid caculations and fitting process, all of which represent 0.1% to 1% size errors which are dwarfed by larger systematic centroid location and other errors from the measurement process. Some of these errors are discussed below.

The MEG and HEG spectra have an opening angle of approximately 9 degrees, and are aligned at the zero order. The true dispersion axis is therefore not exactly the y-axis for either grating. Therefore, the images the centroids of the quadrants are not exactly opposite each other when projected onto the axes. The result is a slight error in the value of $N_y - S_y$ or $B_z - T_z$ in calculating the dispersion direction or cross-dispersion direction separations, and that $N_z - S_z$ & $B_y - T_y$ are not *exactly* zero. For an angle of 4.5 degrees, the $N_y - S_y$ could have a fractional error of as much as $1 - \frac{1}{\cos 4.5} = 0.003$, or 0.3%. The corresponding expected $N_z - S_z$ separation, at a $N_y - S_y$ separation of

5 microns, would be only 0.39 microns. These errors are extremely small and we may ignore this effect. Note that in fitting calculations, the dispersion distances used, $D_{\rm disp}$, are the real distances along the true dispersion axis, and not the projections onto the ACIS y-axis.

As a byproduct of this analysis, the centroids can be used to directly determine the angle between the MEG and HEG spectra. The expected opening angle is 9.934 ± 0.008 degrees.[6] The observed spread from fitting the HEG or MEG order centroids is 9.933 ± 0.002 degrees, which certainly agrees nicely.

A second approximation is that the base of the triangle used to calculate the dispersion direction defocus is the Rowland diameter. While this is true of the zero order, higher orders have a slightly shorter chord (see Fig.2). The upper limit will show this to be a negligible effect: for the farthest orders (80mm from the center) the length of the chord is about 0.5mm less than the Rowland diameter, a change much smaller than 0.1%.

Finally, the Rowland spacing, $X_{\rm RS}$ at XRCF was adjusted from the flight value of 8633.69 mm to 8782.8mm to compensate for finite source distance effects.[2] This creates additional dispersion direction blurring of 1μm.[3]

6. MARX SIMULATIONS

The MARX simulator provides the ability to simulate XRCF shutters, so simulation of these XRCF tests is possible. In addition to setting the shutters appropriately (note the MARX shutter codes differ from the XRCF codes), the following changes need to be made to the marx parameter file to match XRCF finite source and component positions:

- SourceDistance,r,a,537.583,,,"Enter Source distance (meters) (0 if infinite)"
- DetOffsetX,r,a,-194.872,,,"Enter Detector X offset from nominal (mm)"
- RowlandDiameter,r,h,8587.93,1000,,"Enter Rowland Torus Diameter (mm)"

The first change adjusts the source distance from infinity to match the finite source distance at XRCF. The second introduces a detector offset to place the detector at best focus. The third adjusts the total Rowland spacing (Rowland diameter - DetOffset = 8587.93 + 194.872) to the XRCF Rowland spacing of 8782.8mm.

For each XRCF simulation, four MARX v2.11 simulations were run, one for each quadrant. No pileup simulations were made. The results were sequentially concatenated. In this way, an appropriate marx data file was created containing four time intervals, and the complete data set was processed through the same programs as the real data set.

Table 5. MARX Linear Fit Results:

Grating	Defocus (mm)	Tilt (arcmin)
MEG	0.131 ± .002	0.59 ± 0.4257
HEG	-0.150 ± .005	-0.78 ± 0.2544

The MARX results show a $\delta_{\rm MARX} = 0.281mm \pm 0.005$ separation in focus between the MEG and HEG focus points, and show no rotation of the detector about the z axis, as we expect. Not surprisingly, the MARX $N_z - S_z$ and $T_y - B_y$ plots show almost exact agreement with zero (the MARX HRMA and HETG are highly azimuthially symmetric). In addition, the astigmatic defocus values agree extremely well with the theoretical curves predicted from the modified by the primary defocus fit.

Comparing the relative defocus of the MEG and HEG, we see the MARX result agrees to less than one sigma with the fit of the H-HAS-PI-1.003 data:

$$\delta_{1.003,stat} = 0.082 \pm 0.034mm - (-.238 \pm 0.037mm) = 0.320 \pm 0.050mm$$

$$\delta_{1.003,stat} - \delta{\rm MARX} = 0.039 \pm 0.050$$

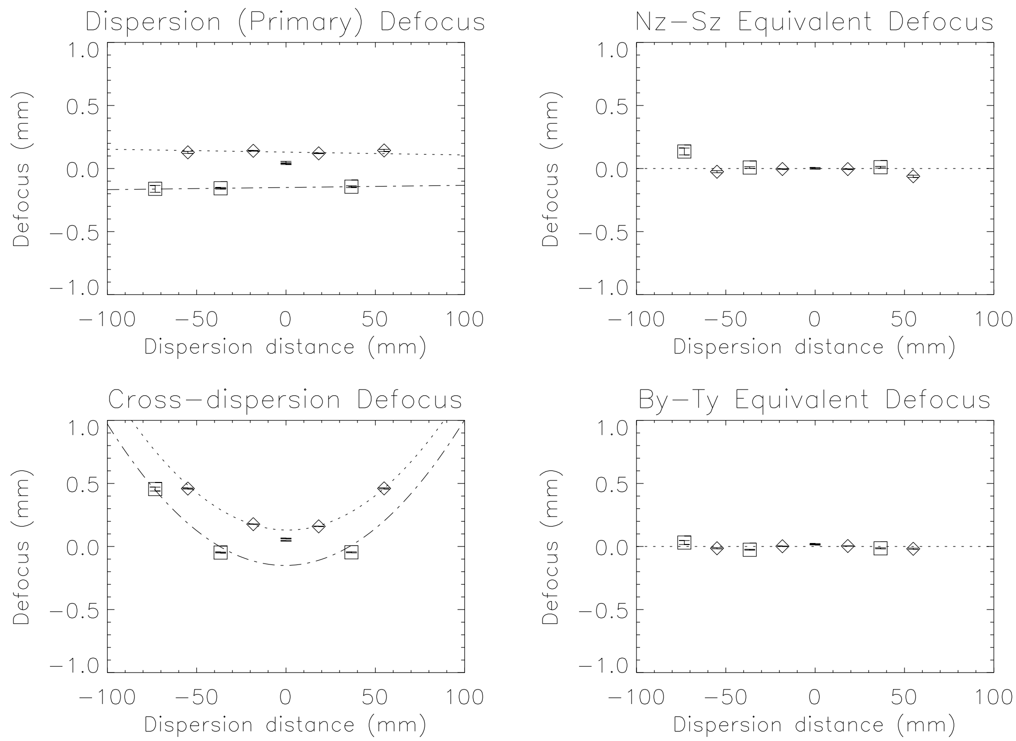

Figure 6. MARX HRMA simulation results. HEG results are plotted as squares and dash-dot lines, MEG results are diamonds and dotted lines. Error bars are statistical errors only. See Fig.5 for explanation of four plots.

7. CONCLUSIONS

The good fits in the MARX simulations indicate the method and the technique are basically sound approaches. While the results clearly suffer from poor statistics, no significant deviations from the expected Rowland geometry were found. While the gaussian fit proved adequate for many orders, in the lowest count histograms there is considerable question about the accuracy of the gaussian mean. Within the limits of these systematic effects, the results of the fits are extremely good.

Given the larger numbers of events in the 1.003 data than the 1.001 data, it would seem the more likely of the two to give reliable results. This hypothesis seems to be supported by the better agreement of the separation of MEG and HEG focus with the simulation results, and the more accurate agreement of the 1.003 cross-dispersion defocuses with the predicted astigmatic curves. With respect to the dispersion direction fits, and in the light of the MARX simulations, we determine that the MEG best focus is located approximately $0.320mm$ in front the the HEG best focus. The ACIS-S appears to have been placed between these two best focuses, and there is indication that the offset to the MEG best focus may even be consistent with zero. Confidence in the tilt measurement is extremely sensitive to the errors in order defocuses, and the systematic error fits indicate that without better statistics in the low count histograms, it is difficult to believe there is any significant tilt of the detector.

Even considering the statistical error estimates, the $N_z - S_z$ and $B_y - T_y$ difference do not show significantly large aberrations of the HRMA/HETG design. When considering systematic errors, there is no indication of aberration.

Ongoing work includes using additional, non-quadrant scan data from XRCF to make additional measurements. For example, while defocus XRCF tests (in which the HETG rings are visible) are useless for determing absolute offsets of the ACIS-S, it may be possible to use such data for additional tilt measurements. The same techniques as used in this paper can be applied to data from the Low Energy Tranmission Grating. In addition, Monte Carlo studies will be employed to better understand the statistical nature of the 1.001 and 1.003 data.

7.1. Acknowledgements

The authors would like to thank Claude Canizares and Herman Marshall for useful discussion and advice.

This work was supported in part by NASA under the HETG contract NAS-38249

REFERENCES

1. D. Dewey, J.J. Drake, R.J. Edgar, K. Michaud, and P. Ratzlaff, "AXAF grating efficiciency measurements with calibrated, non-imaging detectors," *these proceedings*, 1998.
2. D. Dewey, K.A. Flanagan, C. Baluta, D.S. Davis, J.E. Davis, T.T. Fang, D.P. Huenemoerder, J.H. Kastner, N.S. Shulz, M.W. Wise, J.J. Drake, J.Z. Juda, M.Juda, A.C. Brinkman, C.J.Th. Gunsing, J. Kaastra, G. Hartner, and P. Predehl, "Towards the Calibration of the HETGS Effective Area," *Grazing Incidence and Multilayer X-Ray Optical Systems, Proc. SPIE,* Vol. 3113, 1997.
3. H.L. Marshall, D. Dewey, K.A. Flanagan, C. Baluta, C.R. Canizares, D.S. Davis, J.E. Davis, T.T. Fang, D.P. Huenemoerder, J.H. Kastner, N.S. Shulz, and M.W. Wise, "Towards the Calibration of the HETGS Line Response Function," *Grazing Incidence and Multilayer X-Ray Optical System, Proc. SPIE, Vol. 3113*, 160-171, 1997.
4. Daniel J. Schroeder, *Astronomical Optics*, Chapter 14, Academic Press, San Diego, 1987.
5. K.P. Beuermann, H. Bräuniger, and J. Trümper, "Aberrations of a facet-type transmission grating for cosmic x-ray and XUV spectroscopy," *Applied Optics* Vol. 17. No. 15, 98-103, 1978.
6. C.R. Canizares, HETG IPI Team, & ASC., "HETG Ground Calibration: Preliminary Results," MIT, Ver. 1.0, Sept. 30, 1997.
7. M. Bautz, private communication.